Article

Lattice Boltzmann Modelling of Fluid Flow through Porous Media: A Comparison between Pore-Structure and Representative Elementary Volume Methods

Annunziata D'Orazio [1], Arash Karimipour [2] and Ramin Ranjbarzadeh [3,*

[1] Dipartimento di Ingegneria Astronautica, Elettrica ed Energetica, Sapienza University of Rome, Via Eudossiana 18, 00184 Rome, Italy; annunziata.dorazio@uniroma1.it

[2] Department of Mechanical Engineering, Najafabad Branch, Islamic Azad University, Najafabad 8514143131, Iran; arash.karimipour@gmail.com

[3] Dipartimento di Ingegneria Civile, Edile e Ambientale, Sapienza University of Rome, Via Eudossiana 18, 00184 Roma, Italy

* Correspondence: ramin.ranjbarzadeh@uniroma1.it

Abstract: In this study, we present a novel comparison between pore-structure (PS) and representative elementary volume (REV) methods for modelling fluid flow through porous media using a second-order lattice Boltzmann method (LBM). We employ the LBM to demonstrate the importance of the configuration of square obstacles in the PS method and compare the PS and the REV methods. This research provides new insights into fluid flow through porous media as a novel study. The behaviour of fluid flow through porous media has important applications in various engineering structures. The aim of this study is to compare two methods for simulating porous media: the PS method, which resolves the details of the solid matrix, and the REV method, which treats the porous medium as a continuum. Our research methodology involves using different arrangements of square obstacles in a channel including in-line, staggered and random for the PS method and a porosity factor and permeability value for the REV method. We found that the porosity and obstacle arrangement have significant effects on the pressure drop, permeability and flow patterns in the porous region. While the REV method cannot simulate the details of fluid flow through pore structures compared to the PS method, it is able to provide a better understanding of the flow field details around obstacles (Tortuosity). This study has important applications in improving our understanding of transport phenomena in porous media. Our results can be useful for designing and optimizing various engineering systems involving porous media.

Keywords: Lattice Boltzmann modelling; porous media; pore-structure method; porosity factor; fluid flow

1. Introduction

Transport phenomena in porous media are receiving a great deal of attention from many investigators due to their importance in a wide variety of natural and industrial systems. Such systems include electric energy, transportation, construction, metallurgy, food industry, biomedical engineering, groundwater hydrology and oil reservoirs [1,2]. The performance and efficiency of these systems are controlled and/or affected by the movement of fluids, solutes, particles, electrical charges and heat through porous media. Therefore, the characterisation of different transport phenomena through porous media in various engineering structures is pivotal in improving their applications [3].

Regarding numerical simulations, various numerical techniques such as finite difference, finite element, finite volume and spectral methods are conventionally used for the simulations of fluid flow phenomena. Several approaches have been developed to focus on studying fluid flow in porous media [4,5]. In this regard, it is well known that

porosity is one of the most important parameters of a permeable channel. It is often used as an adjustable parameter in models of transport properties through porous media geometries [6,7]. The complex nature of porous media has caused challenges in describing their behaviour in detail. For example, porous media with identical porosity values often have different topologies, and this difference can significantly affect the relationship between their porosity and permeability.

Fluid flows in porous domains are complex fluid-solid systems where the solid matrix is usually fixed. Moreover, they are characterised by a typical multiscale system. Lautenschlaeger et al. [8] proposed a novel model for simulating multi-phase flows in porous media with the lattice Boltzmann method. It integrates two methods to capture fluid interactions at different scales. This model is consistent, accurate, efficient and versatile for various applications involving porous media.

Porous flow is generally modelled by two well-known methods: the Representative Elementary Volume (REV) approach and the Pore-Structure approach. In the REV approach, the porous medium can be seen as a continuum and the fluid flow is characterised by empirical models such as Darcy's law. The REV approach allows us to capture the macroscopic behaviour of the fluid flow without resolving the microscopic details of the pore structure. This method has been widely used and validated in previous studies using LBM for fluid flow in porous media [9,10]. The PS approach thoroughly describes the solid matrix and provides detailed flow information within the pores. This can help to understand the underlying physics of porous flow and its fundamental mechanisms.

Recently, computational fluid dynamics has made significant progress and the lattice Boltzmann (LB) approach is one of the most reliable methods for simulating flow in porous domains. The numerical techniques and approaches can be applied to discretize and solve the Navier–Stokes equations (nonlinear partial differential equations) for fluid flow as a top-down approach. Moreover, the lattice Boltzmann method (LBM) utilizes a bottom-up approach and arrives to recover Navier–Stokes equations as it evolves in the discrete (lattice) space; this evolution can be demonstrated by performing a Chapman–Enskog expansion [11].

One of the important advantages of the LBM is its capability for simulating fluid flow in complex geometries that involve easy construction of boundary conditions in terms of simple rules [12,13]. LBM has proven to be highly efficient in simulating both two and three-dimensional fluid flow applications [14,15].

The applications of the pore-scale approach with LBM can be dated back to 1989 when Succi et al. [16] studied a random porous medium using this method. Soleimani et al. [17] studied heat transfer in channels with extended surfaces and nanoparticles using LBM. They utilized a two-distribution functions model that accounts for the non-homogeneous nanoparticle distribution and compared it with a single-distribution function model that assumes a uniform nanoparticle distribution. They examined how different parameters affect heat transfer and flow dynamics. They proposed a design guideline based on heat transfer enhancement and pressure drop. Similarly, Vasheghani Farahani and Mousavi Nezhad simulated fluid flow in porous media with regular and random packing using LBM. Their study compares the velocity fields and PDFs at different Reynolds numbers and pore structures. It also observes different types of recirculating flow structures in the stagnant zones and the main pathways and discusses their implications for transport phenomena in porous media [18]. Mahmoudi et al. [19] used LBM to investigate pore-scale mechanisms of fluid flow through porous media. They developed a reactive LBM on Quadtree meshes for the first time using the cell-centered approach and discussed the advantages of this scheme. They also studied the effects of dimensionless parameters such as Reynolds, Peclet, Damköhler and Sherwood numbers on the flow and transport phenomena in porous media. Psihogios et al. [20] performed pore-scale simulations of non-Newtonian fluid flows using LBM. To date, pore-scale simulations of flows of simple/complex fluids in porous media are still an active topic of research. Parvan et al. [21] investigated the effect of porosity and topology on LBM's porosity-permeability relationship. They simulated fluid

flow in cases of identical topologies but different porosities to investigate the geometrical effects on fluid flow, as well as in cases of different porosities; along with the porosity factor, the arrangement, shape and size of obstacles are parameters that characterise the structure of porous media geometries [22,23]. With regard to the REV approach with LBM, Feng et al. [24] used the Cascaded lattice Boltzmann (CLB) approach in which the flow field is solved on the D2Q9 lattice by an isothermal CLB model based on the generalised non-Darcy model, while a temperature-based CLB model with the D2Q5 lattice solves the temperature field.

The effect of obstacle geometry on fluid flow is a complex and important topic in many engineering applications, such as thermal fields like heat exchangers. Different geometries can affect the fluid dynamics, such as vortex formation, pressure distribution and drag coefficient. For example, a rectangular obstacle can cause a larger vortex formation than a circular one [25]. Similarly, an angled obstacle can have different aerodynamic coefficients depending on its orientation [26]. Therefore, it is expected that other primitive geometries or even irregular geometries have different effects on the fluid flow than square obstacles. However, the exact nature and magnitude of these effects would depend on several factors, such as the obstacle size, shape, arrangement, porosity, Reynolds number, as well as boundary conditions. A comprehensive study of these factors is beyond the scope of this paper, which focuses on the flow through square obstacles with different arrangements and porosity.

We investigate the effect of porosity ranging from 60 to 95 percent on the fluid flow in porous media. This range of porosity covers a wide spectrum of possible applications of porous media. In this study, we perform 2D fluid flow simulations through porous media, assuming the properties are uniform in the third dimension. This simplifies the computational problem and is valid for some cases with a third-dimensional isotropic, such as cross-flow around tube bundles can be approximated by 2D simulations, as the tubes are aligned along one direction and the flow is mainly perpendicular to it. While 2D simulations are valid for some cases with a third-directional isotropic, for more realistic and complex porous geometries with anisotropic properties, 3D simulations are required to capture the effects of the third dimension on fluid dynamics, such as toroidal and strike-slip motions, asymmetry and pulsation of flow patterns and forces. Indeed, a number of studies have demonstrated that 2D simulations can lead to strong artifacts and may not be representative of the real-world behaviour of porous media [27–29].

In this study, we used a two-dimensional lattice Boltzmann model to simulate Newtonian incompressible fluid flow through a porous medium in a channel for four different porosities. Simulations have been performed by means of both the PS method using a number of obstacles with different sizes, and the REV method. Two methods were employed for simulating porous media: the PS method, which resolves the details of the solid matrix, and the REV method, which treats the porous medium as a continuum. The porosity factor and permeability for each case study in both methods are equal and comparison has been performed in an identical situation, focusing to pressure drop as an effective output parameter. The results provide new insights into fluid flow through porous media as a novel study. The behaviour of fluid flow through porous media have important applications in various engineering structures.

2. Problem Definition

In this study, we model a two-dimensional channel containing porous media using the pore-structure (PS) method and the representative elementary volume (REV) method. Figure 1 shows the different configurations of the porous media part inside the channel. In PS modelling, we simulate fluid flow in three pore-structure geometries with different porosities and calculate their permeability using Darcy's law. In the REV method, we use the porosity and permeability values to define an external force in the lattice Boltzmann method (LBM) that represents the effect of the porous media part. Hence, the pressure drop values are compared to demonstrate the difference between the two methods.
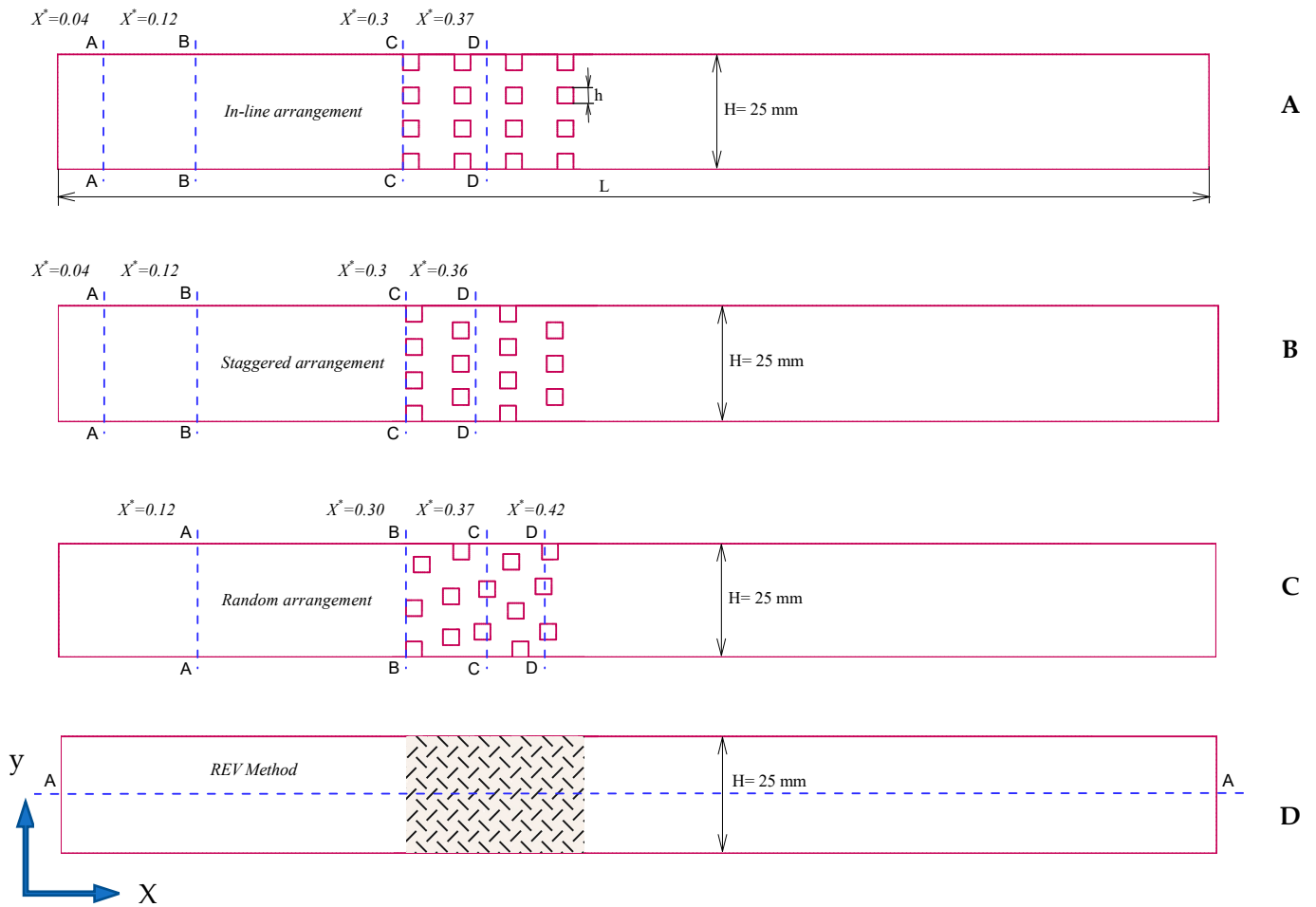
Figure 1. Scheme of different configurations for the pore-structure and the REV methods; In-line (**A**), Staggered (**B**), Random (**C**) and the REV scheme (**D**).

In the first method, we generate a certain number of square obstacles with the same side lengths to create a porous medium and a set of three different pore-structures with porosity factors of 70, 80 and 90 percent. We emphasise that the porosity factors describe just the porous region with obstacles inside the channel, not the entire domain. To change the porosity factor, we vary the dimension of obstacles.

In this study, a uniform fluid flow enters from the channel's left side, and a fully developed velocity field exits at the right side (outlet boundary condition). No-permeable and no-slip boundary conditions are imposed on the walls of the channel and the obstacles.

The porosity of porous media is defined as the ratio of the pores area to the total bulk area of the media (usually expressed as a fraction or percent) [30]. Hence, $\varepsilon = 100$ means there are no blocks in the channel. The total area $A(tot)$ is defined as:

$$A(tot) = A(p) + A(s) \tag{1}$$

where $A(p)$ is the void surface (pore's area) and $A(s)$ is the area of the solid materials; porosity can be expressed as:

$$\varepsilon = \frac{A(p)}{A(tot)} = \frac{A(tot) - A(s)}{A(tot)} \tag{2}$$

Table 1 shows the geometries' properties of the channel and the obstacles geometry, such as h (side length of the obstacles), H (channel width), and L (channel length).

Table 1. Characteristics of the channel with porous part.

Parameters	Value	Dimensions
L	250	mm
H	25	mm
Reynolds number	50	-
h	2.5–3.47–4.4	mm
ε Porosity factor	90–80–70	%

Permeability can be defined by means of Darcy's law or the modified Kozeny–Carman equation. Darcy's law describes a single-phase (fluid) flow in porous media as a benchmark approach [31]. Ignoring the effect of gravity, the following formula is typically used to describe Darcy's law, which is only valid for the laminar fluid flow through a porous medium [32]:

$$K = -\frac{\mu * L}{\Delta p} u \qquad (3)$$

The equation defines the permeability of the medium by K (m^2), μ is the dynamic viscosity $(Pa \cdot s)$ of the fluid, the absolute value of velocity is obtained by $u = Q/A$ $(m \cdot s^{-1})$ and $\Delta p = p_{out} - p_{in}$ is the pressure difference *(Pa)* between the inlet and outlet section of the porous region over a given distance *L (m)*.

Next, we present the physical properties of porous media geometries. In case of the PS approach, obstacles are defined by a solid, impermeable, and no-slip wall; the solid obstacles are square-shaped and arranged in three configurations: in-line, staggered and random. There is no overlap; for applying different porosity factors, the size of blocks is changed. In case of the REV approach, a homogenized porous part was imposed by using the porosity factor and permeability value in the governing equations.

Using a pseudo-random number generator algorithm can be an appropriate approach to achieve a random configuration by randomly placing the obstacles in the domain. Another approach is to use a genetic algorithm or other optimization techniques to find a suitable configuration that satisfies the desired criteria. The choice of approach may depend on the complexity of the simulation and the desired level of randomness in the configuration. However, for the so-called random configuration, we considered the requirements such as equal porosity, obstacles overlapping, shape and the position of the obstacles to generate the third geometry. It should be noted that the configuration is not truly "random". Geometries are generated using a Fortran code.

We show the position of cross sections in the x and y directions on the geometries. They will be used in the results section to show and compare the velocity across the obstacles.

2.1. Governing Equations

In LBM, we solve the fluid flow field using a discrete version of the Boltzmann equation. The LBM approximates the continuous Boltzmann equation by discretising a physical space with lattice nodes and a velocity space by a set of microscopic velocity vectors [33,34]. The discretized velocities system depends on the selected lattice. In this work, we use the D2Q9 approach.

The Boltzmann equation without external force (the first methodology for simulating fluid flow through obstacles) and under the Bhatnagar–Gross–Krook approximation can be formulated as follows [35]:

$$\frac{\partial f_i}{\partial t} + \boldsymbol{c}_i \cdot \nabla f_i = \frac{1}{\tau}(f_i^{eq} - f_i) \qquad (4)$$

The discrete distribution functions evolve on the lattice nodes of the discretized space, satisfying the following evolution equation [33], consisting of the propagation to the neighbouring nodes and a collision process.

$$f_i(\boldsymbol{x} + \boldsymbol{c}_i\delta t, t + \delta t) - f_i(\boldsymbol{x}, t) = -\frac{1}{\tau}\left[f_i(\boldsymbol{x}, t) - f_i^{eq}(\boldsymbol{x}, t)\right] \tag{5}$$

where the subscript i represents the lattice directions around the node, f_i is the discrete Boltzmann distribution function and f_i^{eq} is the equilibrium distribution function; $\boldsymbol{c}_i$ is the microscopic velocity (particle velocity vector) at lattice node $\boldsymbol{x}$ at time t and τ is the hydrodynamic relaxation time, which is a function of fluid viscosity as follows

$$\tau = 0.5 + v\frac{\delta t}{c_s^2} \tag{6}$$

where v is kinematic viscosity, $c_s = \frac{c}{\sqrt{3}}$ is the lattice speed of sound and $c = \frac{\delta x}{\delta t}$ is the velocity at the lattice unit ($\delta x = \delta y = \delta t = 1$). The distance and time step in LBM are denoted by δx and δt, respectively. They are related to the lattice spacing and the time interval between two consecutive collisions of the fictitious particles. The following equation relates the kinematic viscosity to the Reynolds number (Re):

$$v = \frac{u_{lu} \cdot N_y}{Re} \tag{7}$$

The equation shows where u_{lu} is velocity in lattice unit and N_y denotes the number of nodes in y direction.

The equilibrium distribution function is derived from a continuous Maxwellian function; the function is given in the following form for the two-dimensional model with nine microscopic velocity vectors (D2Q9):

$$f_i^{eq} = \omega_i\rho\left[1 + \frac{\boldsymbol{c}_i.\boldsymbol{u}}{c_s^2} + \frac{(\boldsymbol{c}_i.\boldsymbol{u})^2}{2c_s^4} - \frac{(\boldsymbol{u}.\boldsymbol{u})^2}{2c_s^2}\right] \tag{8}$$

The equation defines where ρ is the fluid density at the node, as defined by the density distribution function in the lattice Boltzmann method and ω_i is the weight factor in the ith direction. The lattice Boltzmann method considers the fluid flow domain as discrete particles that move on a regular lattice and collide with each other according to some rules [34]. Here, the following equation expresses the weight factors for the D2Q9 LBM:

$$\begin{cases} \omega_i = \frac{16}{36} \ (i = 0) & \text{For rest particle} \\ \omega_i = \frac{4}{36} \ (1 \leq i \leq 4) & \text{For particles streaming to the face connected neighbours} \\ \omega_i = \frac{1}{36} \ (5 \leq i \leq 8) & \text{For particles streaming to the edgeconnected neighbours} \end{cases} \tag{9}$$

The weight factors are derived based on the lattice type (D2Q9). The following equation defines the discrete velocities based on the D2Q9 model [36]:

$$\boldsymbol{c}_i = \begin{cases} (0,0) \rightarrow & i = 0 \\ \left(cos\frac{\pi(i-1)}{2}, \ sin\frac{\pi(i-1)}{2}\right) \rightarrow & i = 1 - 4 \\ \sqrt{2}\left(cos\frac{\pi(2i-9)}{4}, \ sin\frac{\pi(2i-9)}{4}\right) \rightarrow & i = 5 - 8 \end{cases} \tag{10}$$

The macroscopic variables of fluid flow, such as density ρ, velocity $\boldsymbol{u}$ and pressure p are calculated using the following relations:

$$\rho = \sum_{i=0}^{8} f_i \tag{11}$$

$$\rho \boldsymbol{u} = \sum_{i=0}^{8} c_i f_i \tag{12}$$

$$p = c_s^2 \rho \tag{13}$$

External forces can be taken into account by adding forcing terms in the evolution equation.

It can be demonstrated that the following macroscopic set of equations can be derived using the Chapman–Enskog expansion in the limit of a small Mach number, for more details see this reference [33]. The following equations show the continuum and momentum equations:

$$\nabla . \boldsymbol{u} = 0 \tag{14}$$

$$\frac{\partial \boldsymbol{u}}{\partial t} + (\boldsymbol{u}.\nabla)\left(\frac{u}{\varepsilon}\right) = -\frac{1}{\rho}\nabla(\varepsilon p) + v_e \, \nabla^2 \boldsymbol{u} + \boldsymbol{F} \tag{15}$$

The equation shows where ρ is the fluid density, $\boldsymbol{u}$ and p are the apparent velocity and pressure, v_e is the effective viscosity, $\boldsymbol{F}$ is the total force including both the medium resistance and external forces,

$$\boldsymbol{F} = -\frac{\varepsilon v}{K}\boldsymbol{u} - \frac{\varepsilon F_\varepsilon}{\sqrt{K}}|\boldsymbol{u}|\boldsymbol{u} + \varepsilon \boldsymbol{G} \tag{16}$$

where v is the fluid viscosity and $\boldsymbol{G}$ is the external body force. The structure function F_ε depends on the permeability K and the porosity ε. The first part on the right side describes Darcy's term, and the second part represents Forcheimer's term (here, $\boldsymbol{G} = 0$). In this work, the term $\boldsymbol{F}$ as total external force consists of only a linear term (Darcy's term).

In order to simulate the porous media by means of the REV method [37], a porosity factor was introduced into the equilibrium distributions and the effects of viscous and inertial flow resistance in the porous medium were incorporated in the form of force terms in Boltzmann's equation as follows:

$$f_i(\boldsymbol{x} + \boldsymbol{c}_i \delta t, \, t + \delta t) - f_i(\boldsymbol{x}, t) = -\frac{f_i(\boldsymbol{x}, t) - f_i^{eq}(\boldsymbol{x}, t)}{\tau} + \delta t F_i \tag{17}$$

where,

$$F_i = w_i \rho \left(1 - \frac{1}{2\tau}\right) \left[\frac{\boldsymbol{c}_i \boldsymbol{F}}{c_s^2} + \frac{\boldsymbol{u}\boldsymbol{F} : (\boldsymbol{c}_i \boldsymbol{c}_i - c_s^2 \boldsymbol{I})}{\varepsilon c_s^4}\right] \tag{18}$$

In this model, the equilibrium distribution function was defined as:

$$f_i^{eq} = \omega_i \rho \left[1 + \frac{\boldsymbol{c}_i . \boldsymbol{u}}{c_s^2} + \frac{\boldsymbol{u}\boldsymbol{u} : (\boldsymbol{c}_i . \boldsymbol{c}_i - c_s^2 \boldsymbol{I})}{2\varepsilon c_s^4}\right] \tag{19}$$

The macroscopic fluid volume-averaged density is given by,

$$\rho = \sum_{i=0}^{8} f_i \tag{20}$$

Additionally, the fluid velocity was defined as,

$$\rho \boldsymbol{u} = \sum_{i=0}^{8} \boldsymbol{c}_i \, f_i + \frac{\delta t}{2} \rho \boldsymbol{F} \tag{21}$$

The general form of an external force with considering the non-linear term in the channel has been described in Equation (16).

Because of the strong non-linearity of Equation (16) together with (21), Guo and Zhao [10,33] suggested using a temporal velocity (v), to incorporate the presence of porous media. Then, the fluid velocity can be calculated as

$$u = \frac{v}{L_0 + \sqrt{L_0^2 + L_1|v|}} \tag{22}$$

Here, the temporal velocity (v) and two parameters can be determined as,

$$v = \frac{\sum_{i=0}^{8} c_i \, f_i}{\rho} + \frac{\delta t}{2}\varepsilon G \tag{23}$$

$$L_0 = \frac{1}{2}\left(1 + \varepsilon \frac{\delta t}{2}\frac{v}{K}\right) \tag{24}$$

$$L_1 = \varepsilon \frac{\delta t}{2}\frac{F_\varepsilon}{\sqrt{K}} \tag{25}$$

Here, L_0 and L_1 are two constant parameters, F_ε denotes the geometric function and can compute by

$$F_\varepsilon = \frac{1.75}{\sqrt{150\varepsilon^3}} \tag{26}$$

The simulation consists of three major phases. The initial conditions of the simulation are set in the first phase; to increase the computational efficiency, the relaxation time is set to unity, resulting in the non-equilibrium distribution function initially being equal to the equilibrium distribution function.

In the second phase, the propagation of the distribution function to the neighbouring nodes and the collision process are performed, then assigning boundary conditions. Each node's new density and macroscopic velocity for the next time step are computed.

The third phase involves calculating new equilibrium distribution functions for the final calculation and checking the criteria value.

2.2. Boundary Conditions at the Domain and Solid Nodes in the D2Q9 Approach

At the domain boundary, specific components of the distribution function (i.e., inlet, outlet, top and bottom nodes and obstacles boundaries) are unknown, as shown in Figure 2. These unknown components are calculated from the known components by setting appropriate constraints depending on the desired boundary condition.
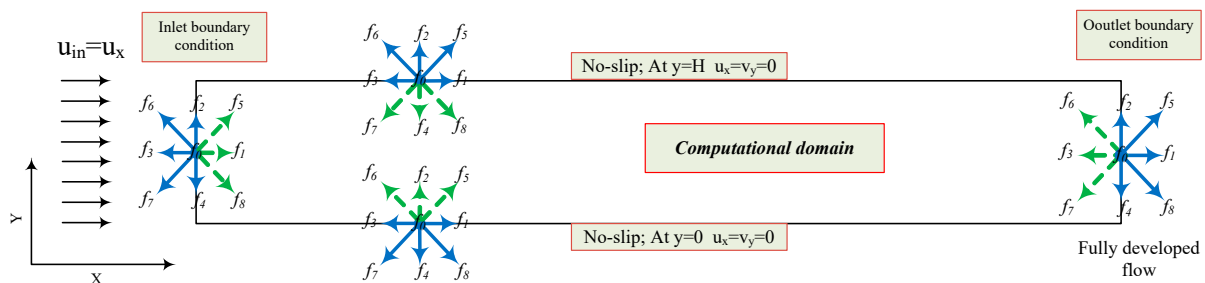
Figure 2. Different domain boundary conditions for the channel. The unknown components are shown in green colour and the known ones in blue.

If the spatial derivative of the velocity on the boundary is prescribed, the velocity boundary condition can be assigned to the boundary. This boundary condition is known as the Zou/He [38] boundary condition and can be used to model inflow and outflow boundaries. The boundary nodes are "wet nodes" since they can be thought of as representing the last physical fluid particle adjacent to the wall and so are "fluid". For the D2Q9 lattice,

constraints to construct the velocity boundary condition are the zero and first-order discrete moments of the distribution function.

The components f_1, f_5 and f_8 at the inlet boundary are calculated from the known components f_2, f_4, f_3, f_6, f_7 and f_0 and inlet velocity at the same position.

To calculate the outlet unknowns f_3, f_6 and f_7, which come from outside the computational domain, we use an extrapolation scheme. The unknown distribution functions at the x-last node (*n*) on the right side of the channel are calculated using the following second-order extrapolation relationship:

$$f_i(\boldsymbol{x}_n, t) = 2f_i(\boldsymbol{x}_{n-1}, t) - f_i(\boldsymbol{x}_{n-2}, t) \tag{27}$$

An on-grid bounce back is applied for the solid walls (top and bottom walls of the channel and obstacles walls) [39]. The unknown components on the solid surfaces can be defined as:

$$Full-way: \ f_{\bar{i}}(\boldsymbol{x}, t + \delta t) = f_i(\boldsymbol{x}, t) \tag{28}$$

Note that $\bar{i}$ is the inverse direction to *i*. The final relations for all boundaries are provided in Table 2.

Table 2. Relations for computing unknowns on boundaries for the D2Q9 model.

Boundaries	Known Components		Unknowns		Relations	
Inlet	u_x, u_y, f_0, f_2, f_4, f_3, f_6, $f_7 \rho$, f_1, f_8, f_5				$\rho_{in} = \frac{1}{1-u_x}[f_0 + f_2 + f_4 + 2(f_3 + f_6 + f_7)]$ $f_1 = f_3 + \frac{2}{3}\rho u_x$ $f_8 = f_6 + \frac{1}{2}(f_2 - f_4) + \frac{1}{6}\rho u_x - \frac{1}{2}\rho u_y$ $f_5 = f_7 - \frac{1}{2}(f_2 - f_4) + \frac{1}{6}\rho u_x + \frac{1}{2}\rho u_y$	
Outlet	f_0, f_2, f_4, f_1, f_5, f_8		f_3, f_6, f_7		$f_3 = 2f_{3,m-1} - f_{3,m-2}$ $f_6 = 2f_{6,m-1} - f_{6,m-2}$ $f_7 = 2f_{7,m-1} - f_{7,m-2}$	
Bottom	u_x, u_y, f_0, f_1, f_3, f_4, f_7, $f_8 f_2$, f_5, f_6				$f_2 = f_4$ $f_5 = f_7$ $f_6 = f_8$	
Top	u_x, u_y, f_0, f_1, f_2, f_3, f_5, $f_6 f_4$, f_7, f_8				$f_4 = f_2$ $f_7 = f_5$ $f_8 = f_6$	
On the obstacles	**Top side**	**Bottom side**		**Left side**		**Right side**
	$f_2 = f_4$ $f_5 = f_7$ $f_6 = f_8$	$f_4 = f_2$ $f_7 = f_5$ $f_8 = f_6$		$f_3 = f_1$ $f_5 = f_7$ $f_6 = f_8$		$f_4 = f_2$ $f_8 = f_6$ $f_1 = f_3$

2.3. Lattice Grid Independency and Validation

The lattice grid independency of the solution was evaluated for the first case in Figure 1 to select the appropriate lattice grid. Different lattice grids included 75∗750, 150∗1500, 300∗3000 and 500∗5000 in y and x directions, respectively. The comparison of the velocity profiles at x/L = 0.30 and x/L = 0.37 sections for the in-line configuration are shown in Figure 3.
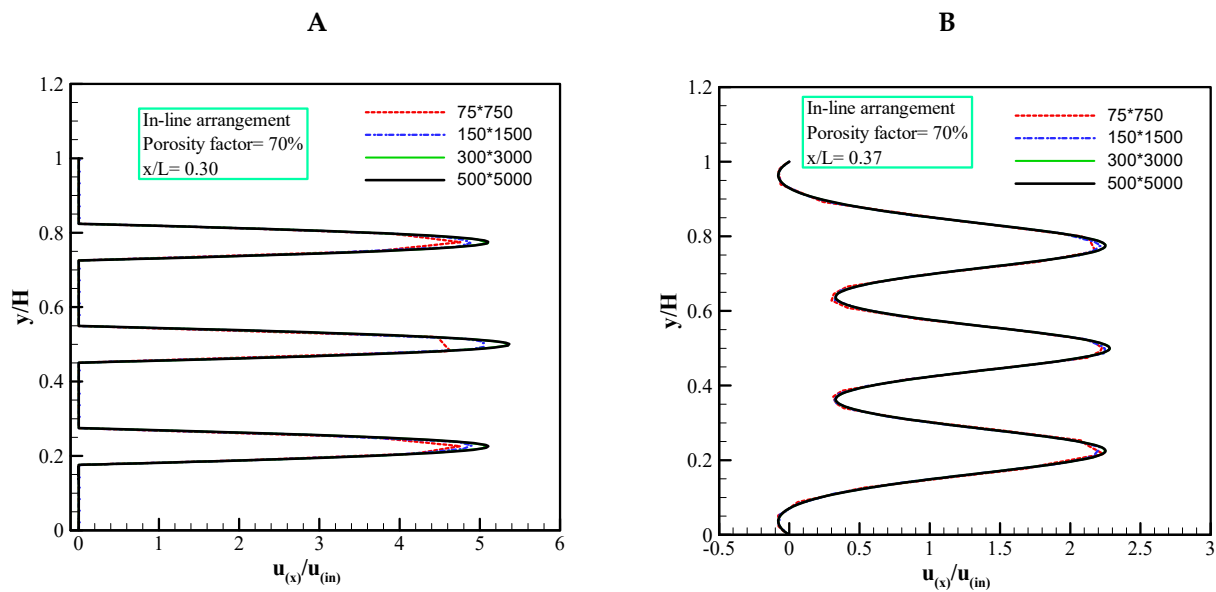
Figure 3. Dimensionless x-velocity distribution through In-line obstacles at Reynolds Number 50; Positions x/L = 0.3 (**A**) and x/L = 0.37 (**B**).

We compared the dimensionless x-velocity at different lattice nodes and calculated the maximum difference using the following relationship. Table 3 shows the details. The results indicate that the first and second lattice nodes are inaccurate for the lowest porosity, while the third and fourth grid sizes have no significant difference.

Table 3. Lattice grid study calculations for in-line arrangement at porosity factor=70%.

| Re	Number of Lattice Nodes	Error (%) Error $= \frac{|U_{new}-U_{old}|}{U_{new}} *100$
50	$75 * 750$ $150 * 1500$ $300 * 3000$ $500 * 5000$	3.45 1.7104 0.074

The results showed less than a 1% difference between the grid size of $300 * 3000$ and $500 * 5000$. It is concluded that the grid of $300 * 3000$ provides a good compromise between precision and calculation time.

3. Result and Discussion

This study presents the fluid flow simulation through the porous medium using the PS and the REV methods; in the pore-structure method, different arrangements such as in-line, staggered, and random are modelled. The porosity factor was changed by increasing the dimension of square obstacles in pore-structure modelling. There are various arrangements, but the porosity is the same for all. All case studies were simulated at Re = 50 with the same boundary conditions for both methods. In the following sections, the obtained results are presented.

- **Streamline plots of the velocity field for different arrangements**

The effect of different configurations on streamlines inside the channel for a selected porosity factor is shown in Figure 4. The porosity factor is fixed at 80 percent for all geometries.
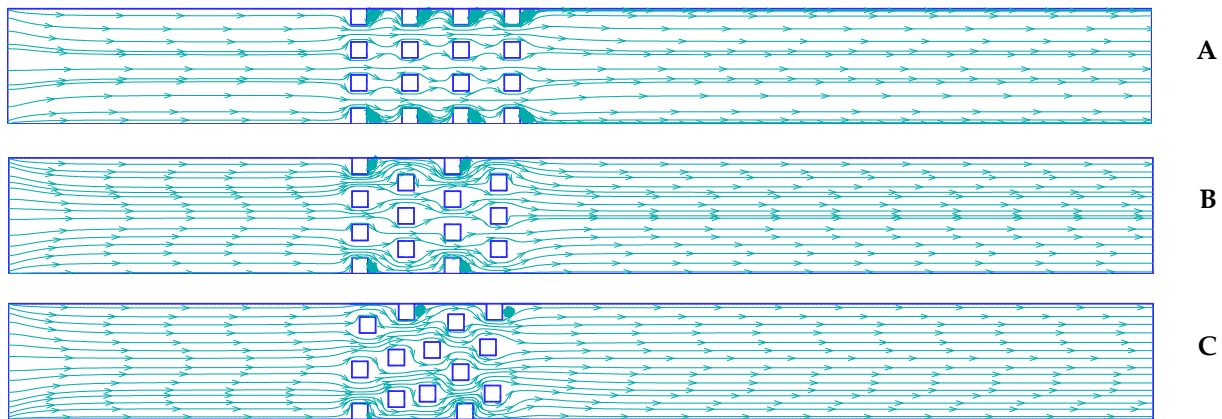
Figure 4. Streamline patterns for different configurations, including In-line (**A**), Staggered (**B**) and Random (**C**) at Reynolds number = 50 and Porosity = 80.

As the flow was approaching the obstacles, the streamlines were compacted. Therefore, near the obstacles, the streamlines were denser. It can be seen that there was a weak circulation eddy behind the obstacles that were near the bottom and top walls. Different arrangements did not significantly affect the streamlines at a constant porosity because there was no very tight passage or a compact pass for fluid flow; in contrast, it can occur in low porosities. Minimal negative values emerged due to the circulation of the flow behind the objects.

It can be found that the velocity distribution of the in-line and staggered structures was relatively concentrated and very uniform. In contrast, the random form's velocity distribution was nonuniform, with different velocity peaks at the pores.

It is demonstrated that the frequency of the flow recirculation in the wake of the obstacles decreased as the arrangement became random (see random arrangement streamline graph, C). This is because the random arrangement created more irregular and asymmetric flow structures that interfered with each other and reduced the formation of coherent vortices. As can be seen from the figure, the flow recirculation was more frequent and regular for the inline and staggered arrangements than for the random arrangement, which confirms our qualitative observation.
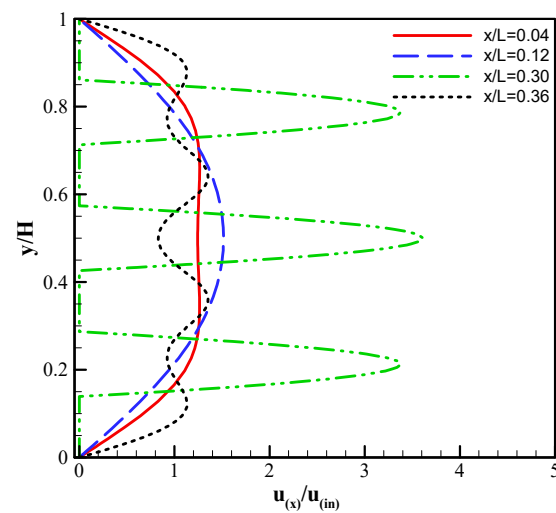
- **Velocity profiles at different cross-sections**

The dimensionless longitudinal velocity profiles at different cross-sections of the channels are shown in Figure 5. The position of these sections is shown on the geometries in Figure 1. They are located at the entrance region of the channel, at the entrance section of the porous part and into the porous region.

We compared velocity profiles at different sections within the same arrangements. This allowed us to examine how the velocity distribution varied at different positions in the channel under the same flow conditions. Furthermore, different sections were chosen to demonstrate velocity behaviour in different positions of the channel, such as the entrance region (shown for all cases), the position that borders the first column of obstacles (shown for all cases), the middle of the obstacles, etc. Evaluating the velocity distribution at these different positions provided important insights into the flow dynamics of the system.

Fluid flow was fully developed at $x/L = 0.12$, then it entered to the porous part. It is observed that some low-velocity zones were formed in porous parts due to boundary-layer separation. On the contrary, there was a very high-velocity zone between the obstacles, $x/L = 0.3$ for A and B cases. The effect of the presence of the porous medium becomes more evident with velocity line graphs at cross-sections of obstacles. The highest value of the dimensionless x-velocity showed in the third cross-section $x/L = 0.3$ for in-line and staggered arrangement geometries; its value was $u_x/u_{in} = 3.64$.
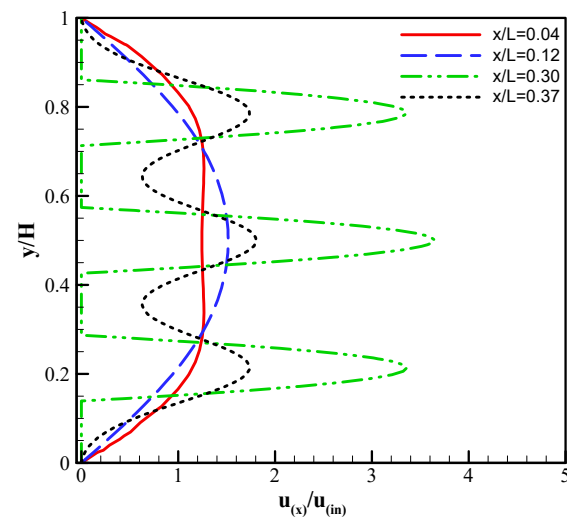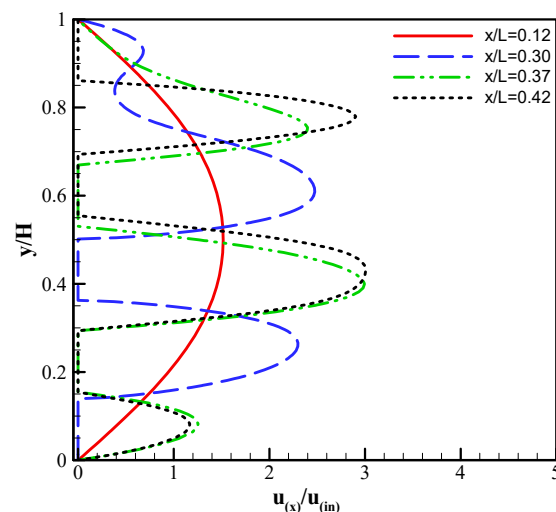
Figure 5. Dimensionless **x**-velocity distribution through the channel at different cross sections, porosity = 80%.

The results in Figure 5 show that the obstacle arrangements influence the velocity distribution. As can be seen, the in-line and staggered arrangements have more uniform and predictable velocity patterns than the random arrangement. This is because the obstacles in the regular arrangements create periodic flow structures that facilitate the momentum

transfer and increase the local velocities. However, in a random arrangement, the obstacles create more complex and chaotic flow structures that reduce the momentum transfer and decrease local velocities.

- **The effect of the porosity factor on the velocity field**

The effect of various obstacle sizes on the velocity field is shown in Figure 6 in terms of streamlines and velocity contours in the case of configuration B (staggered obstacles) for three values of porosity factor (90%, 80%, 70%).
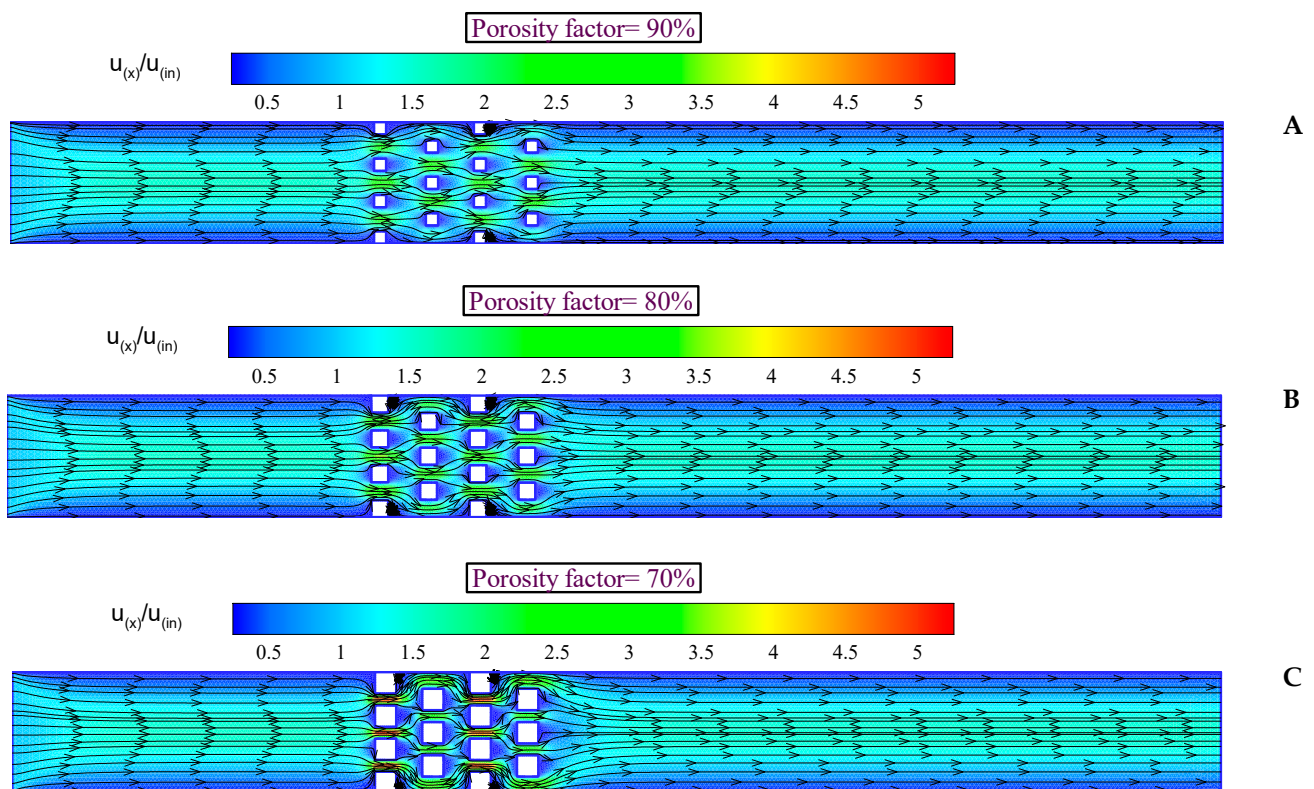
Figure 6. Streamline and velocity contours for Staggered arrangement with different porosities including (**A**) 90%, (**B**) 80% and (**C**) 70% at Reynolds number = 50.

As the size of the obstacles increased, the porosity factor decreased. The porosity factor is the ratio of the pore area to the total area of the porous domain. When the porosity factor decreased, the pore area becomes smaller and the flow resistance increased. This caused the flow to separate more sharply from the edges of the blocks, creating stronger and longer vortices behind them. The strength and length of vortices are proportional to the local Reynolds number, which is a function of both the pathway width and the flow velocity. When the porosity factor decreased, the pathway width also became smaller and the flow velocity increased due to conservation of mass. Therefore, when the porosity factor decreased, the local Reynolds number increased, resulting in stronger and longer vortices. The minimum velocity values occurred due to flow circulation behind the obstacles in the case with the lowest porosity. This is consistent with previous studies [40,41].

The velocity ratio and the pattern of streamlines do not change much when the channel contains a high-porosity medium (smaller obstacles). This means that the pressure drop in the channel does not increase due to the high-porous medium compared to the low-porous medium cases. This result can be seen by comparing different porosity parts inside the channel. A high-porosity case has less resistance to the fluid flow and thus does not affect the velocity or pressure distribution significantly. On the other hand, a low-porosity medium (larger obstacles) creates more turbulence and drag in the flow, resulting in a higher pressure drop and a lower velocity ratio.

The contours show that the streamlines near the walls of the channel or obstacles in the porous zone are more compact. In other words, the velocity contours become denser with decreasing porosity factor. It can be concluded that the effects of the velocity gradient near the walls of the channel become more significant as the value of the porosity decreased, which in turn increased the rate of pressure drop.

- **Velocity profiles through the central axis of the channel**

Figure 7 shows the longitudinal velocity along the x-axis of the channel at position $y = H/2$, for the configurations A, B and C for three values of porosity factor. This position is important because it allows us to compare the velocity profiles of different configurations and porosities, as they have the same initial and boundary conditions. Fluid flow with a uniform velocity profile enters the channel after developing through the hydrodynamic entrance region, then it enters the porous part as a developed fluid flow. When it reaches the first obstacles, it diverts from the straight path and moves toward the blocks with different arrangements, which leads to an increase in velocity. In this case, the high-velocity regions are created between the obstacles. By decreasing the porosity factor to 70%, the velocity increased rapidly. After passing the porous region, the fluid flow reached its fully developed situation. Based on the velocity pattern, it seems that the first case study should have the highest pressure drop and the third geometry the lowest one. This is because the in-line arrangement has a shorter distance between all block columns, while fluid flow in the random configuration can pass through the obstacles more easily. The maximum velocity was enhanced by decreasing the porosity factor in all cases. The arrangement of obstacles is an essential factor in controlling the maximum velocity.

Figure 8 presents a comparison of dimensionless normalized velocity along the channel. The porosity factor for all cases was fixed at 80%. Different configurations have a specific pattern with an increasing and decreasing trend; the highest value was for the in-line configuration, while the lowest velocity was reported for the random arrangement. The results show how different configurations affect the flow resistance and cause the pressure drop in porous media. It is shown that the value of velocity changed subsequently after the obstacles in the porous part for redistribution, as in Poiseuille flow.

In Figure 9, pressure drop results across the porous region for all configurations are reported for four values of porosity factor. As one can see, the highest pressure drop occurs in case of the in-line arrangement. It is clear that more obstacles in one column occupying the section in the porous region cause higher resistance to the flow and lead to higher pressure drop. It can be said that a viscous layer surrounds the obstacles, which leads to the creation of an adverse pressure gradient behind the blocks.

As the arrangement of obstacles is changed, from in-line to staggered and then to a random one, the pressure drop decreases significantly, mainly for larger obstacles size. Naturally, the resistance force reduces at lower obstacles size, resulting in passing flow through it quickly.

By increasing the porosity to higher values (90% and then 95%), the pressure drop for all cases is almost very close to each other because the effect of resistant force decreases and the fluid can flow through the porous part without high geometrical effects.

As shown, the distribution of irregular structures and larger pores enables most of the fluid flow with relatively better permeability. Conversely, the solid in-line structure causes a higher pressure drop and lower permeability than other arrangements. In the case of the lowest porosity factor [42], the pressure drop in the in-line geometry was more than double compared to the random arrangement, so a regular and uniform pore structure can cause higher fluid flow resistance than the staggered and random configurations.
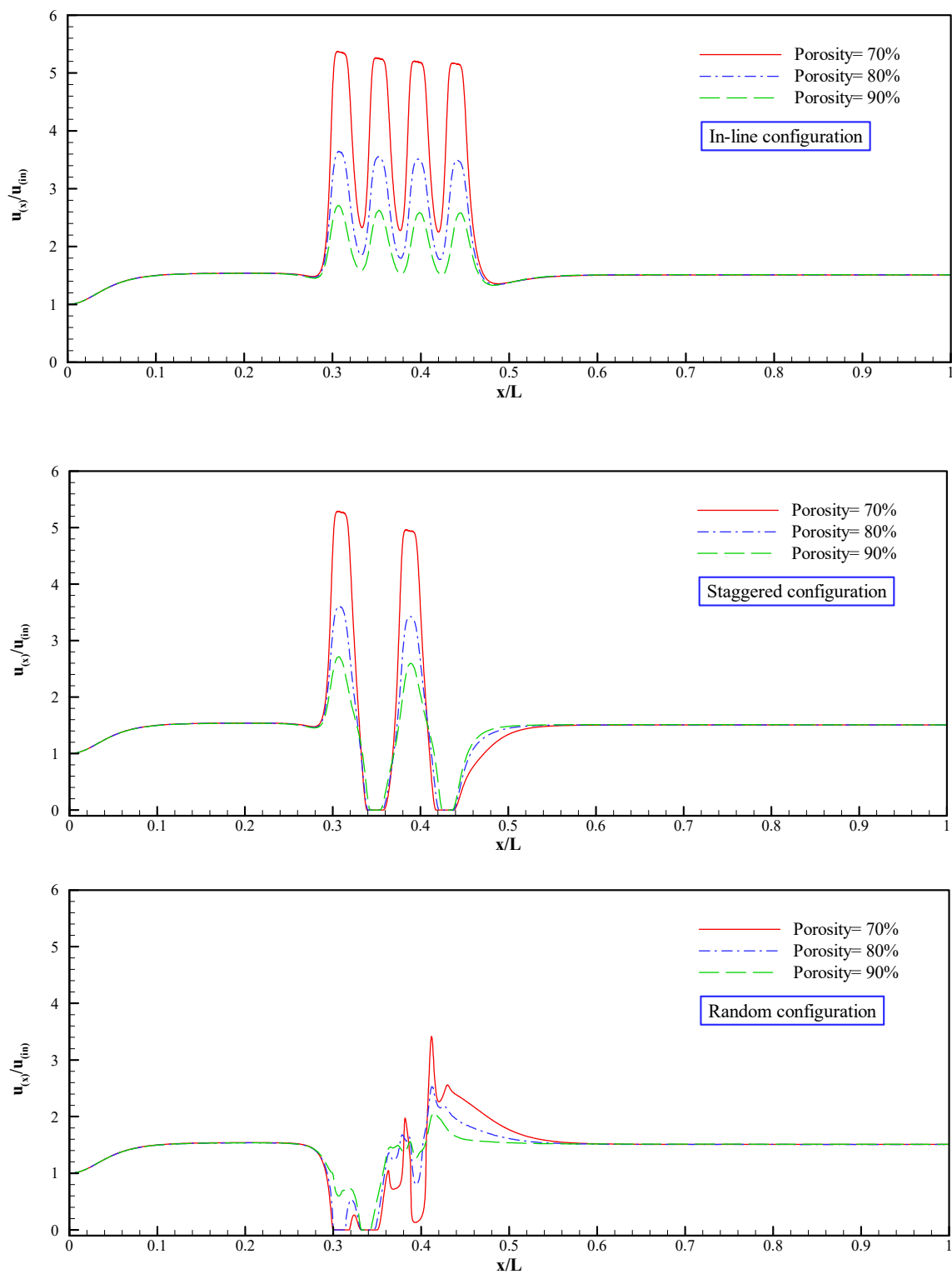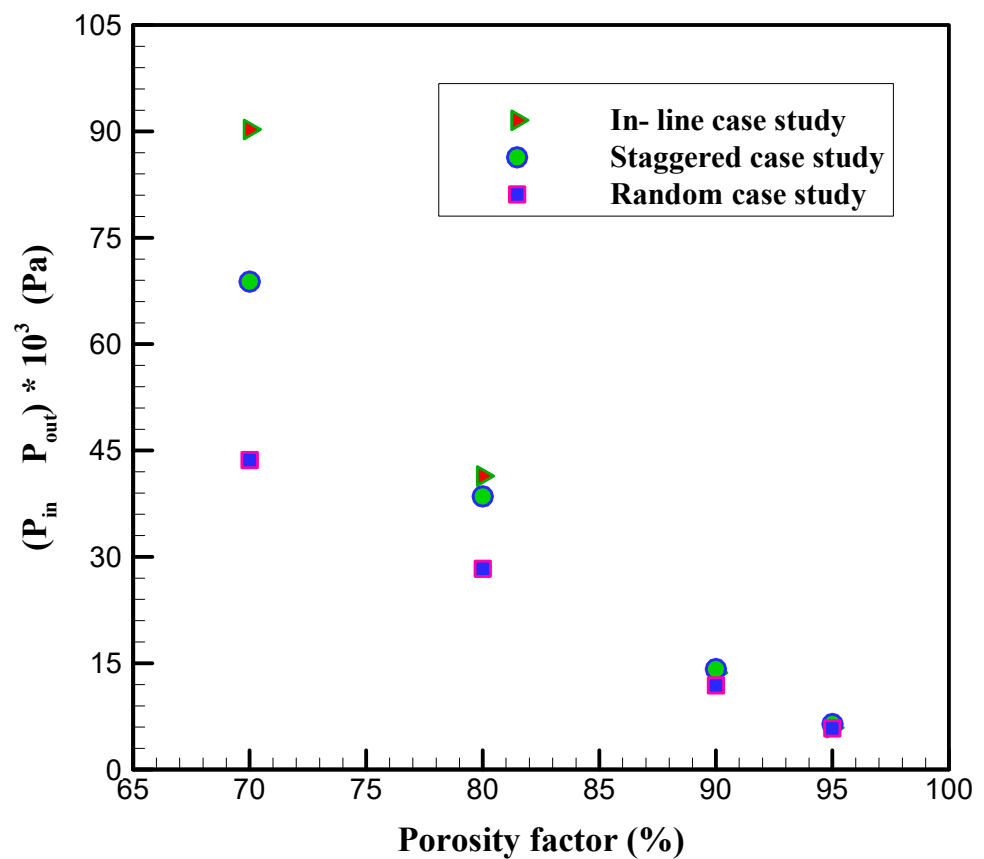
Figure 7. Velocity distribution in the central axis for all cases with different porosities; The effect of changing the porosity on velocity distribution in the centerline for (**A**) In-line, (**B**) Staggered and (**C**) Random arrangements.
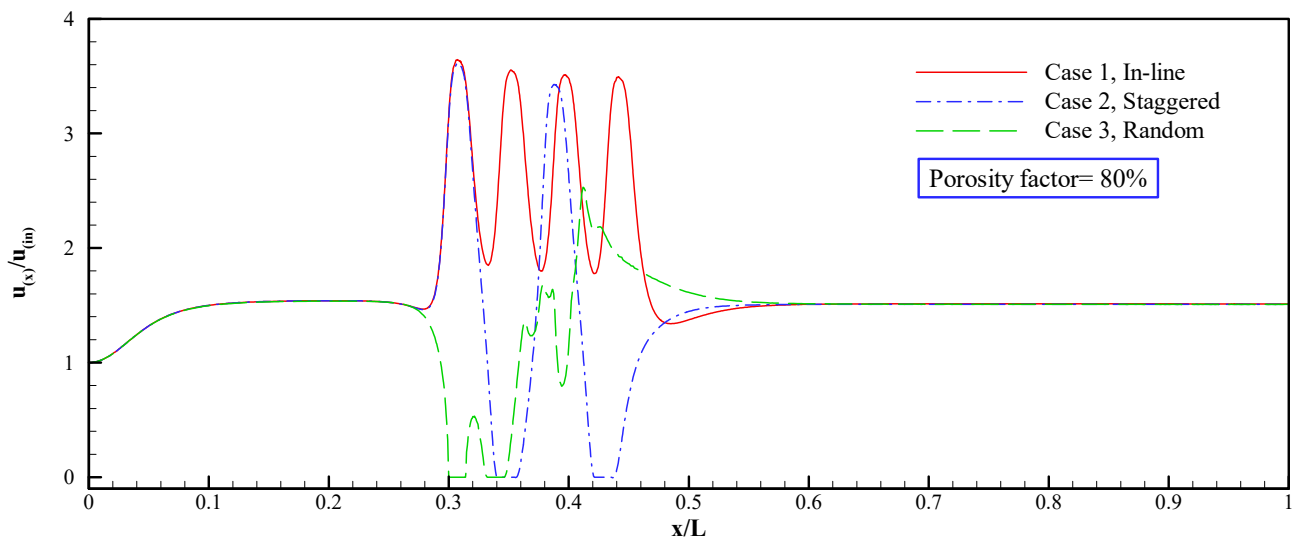
Figure 8. Comparison between x-velocity distribution in the x-axial direction for different configurations, porosity= 80%.


Figure 9. The results of pressure drop through the test section (Porous part) for different geometries with different porosities.

- **The second method for simulation of porous media; using obtained results in pore-structure for re-modelling by the REV method**

  In this section, we present the results obtained by the representative elementary volume (REV) method. Moreover, to compare this method with the PS method, we use pressure drop results as an important output. We modelled three different obstacle configurations using the PS method and we used the same porosity and permeability values in the PS simulation to define each porous medium (in the REV method) as an external force in the lattice Boltzmann method that represents the effect of the porous media part. We used Darcy's law to calculate the permeability value of each case.

  Figure 10 presents a longitudinal velocity contour corresponding to the in-line arrangement with a porosity of 70%.

u_x/u_{in}
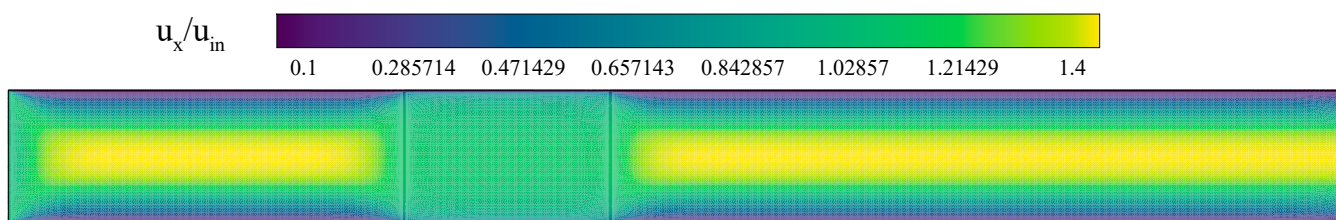
Figure 10. The contour plot of velocity distribution in a channel with porous part, simulated by the REV method.

- **Comparison between Pore- Structure and REV methods in terms of pressure drop results**

  We compared the Pore-Structure and the REV methods for modelling equal case studies with the same porosity and permeability. The REV method gave higher pressure drop results than the Pore-Structure method in all cases. We used in-line, staggered and random arrangements with porosity factors of 70, 80, 90 and 95 percent for the Pore-Structure cases. We calculated permeability by Darcy's law after modelling the case studies by the Pore-Structure method. For the REV method, we defined the porous part using Darcy's term as an extra term to standard lattice Boltzmann method. Finally, we compared the results for the same porosity and permeability values. Table 4 summarizes the comparison results.

Table 4. Pressure drop difference between PS and REV method using Darcy's law.

Porosity		70%	80%	90%	95%
Pressure drop difference (%)	In-line	3.04	4.61	9.09	11.02
	Staggered	2.84	4.82	7.09	9.37
	Random	3.91	6.42	10.21	11.87

The in-line arrangement generated the highest pressure drop and the random one generated the lowest one because of the geometrical resistance.

The difference, *E* %**,** between the pressure drop obtained by the REV method and the PS simulations (as defined in Equation (29)) ranges from 2.84% to 11.87%, with more considerable values for higher porosities.

$$E\% = 100 * \frac{|\Delta P_{REV} - \Delta P_{Pore-stucture}|}{\Delta P_{REV}} \tag{29}$$

One of the influential parameters for the flow is the tortuosity factor, which accounts for the difference related to the different arrangements. By means of the REV method, we cannot detect nor impose the geometrical effect on the equations for modelling porous medium, since in the REV method permeability is placed into the equations as a computed

parameter from PS-modelling. In order to evaluate the tortuosity effect on velocity and pressure fields, future works will be performed.

4. Conclusions

In this paper, we employed a two-dimensional lattice Boltzmann model to simulate fluid flow through porous media using two different methods: the pore-structure (PS) and the representative elementary volume (REV). We compared the pressure drop and velocity profiles for different porosities and arrangements of square obstacles in a channel as a novel study. Our main findings are:

1. We have evaluated the results regarding streamlines, velocity profiles, and pressure drop results for different porosities and configurations, including in-line, staggered and random.
2. We demonstrated that the PS method can capture the true details of the fluid flow through the pore structures compared to the REV method, which assumes a homogenized porous region with a constant porosity factor and permeability value.
3. Comparison in terms of pressure drop between the methods shows that the REV method gives a similar pressure drop behaviour and values to the PS method (with a percent error between 2.84 and 11.87), and the difference was higher for higher porosities. This difference is related to the lack of a geometrical parameter in the empirical permeability equations.
4. The tortuosity can affect the pressure drop and hence the permeability of the porous media. We have observed that different arrangements of obstacles can result in different streamline patterns (tortuosity) for the same porosity degree.
5. The porosity factor and the arrangement of obstacles significantly affect the pressure drop and the flow field in the porous region. The lower porosity factor (70%) leads to more extensive and robust vortexes near the walls, which are effective for increasing the pressure drop. Additionally, the regular arrangement of obstacles causes a more significant resistance and a higher pressure drop.

The original findings contribute to a better understanding of the transport phenomena in porous media, which is essential for many engineering applications such as energy, transport in different heat exchangers. In addition, they can improve the design and performance of these systems.

We have demonstrated the advantages and limitations of PS and REV methods for modelling porous flow using LBM. We have also shown how different geometrical parameters can influence flow characteristics and transport properties as novel research.

For future research, we suggest extending our study to three-dimensional simulations, which can account for more realistic and complex porous geometries with anisotropic properties. We also recommend exploring other types of obstacles, such as circular or irregular shapes.

Author Contributions: Conceptualization, A.D., A.K. and R.R.; methodology, A.D., A.K. and R.R.; software, A.D., A.K. and R.R.; validation, A.D., A.K. and R.R.; formal analysis, A.D., A.K. and R.R.; investigation, A.D., A.K. and R.R.; resources, A.D.; data curation, A.D., A.K. and R.R.; writing—original draft preparation, Ranjbarzadeh; writing—review and editing, A.D., A.K. and R.R.; visualization, A.D., A.K.and R.R.; supervision, A.D. and A.K.; project administration, R.R.; funding acquisition, A.D. and R.R. All authors have read and agreed to the published version of the manuscript.

Data Availability Statement: Data can be provided by the authors upon request.

Conflicts of Interest: All authors declare that they have no conflict of interest.

Nomenclature

Greek Symbols

A_c	Area of the obstacle m^2
c	Lattice speed
c_s	Lattice speed of sound
Da	Darcy number
e	Discrete velocity vector or streaming speed for single particle
f	Density distribution function
f^{eq}	Equilibrium density distribution function
F	Total External force
F_ε	Geometric function
G	External force
h	Side length of the obstacles
H	Channel width m
I	Unit tensor
K	Permeability, m^2
L	Length of the channel m
P	Pressure
q_r	Volumetric flow rate
Q	Number of microscopic velocity vectors
Re	Reynolds number, $u_{in}2H/\nu$
t	Time s
u_{in}	u-component at the channel inlet m s^{-1}
u, v	Velocity components m s^{-1}
x, y	Cartesian coordinates m
w	Weight factor

Greek Symbols

β	Forchheimer coefficient/Beta factor
δx	Lattice spacing
δy	Lattice spacing
Ω	Collision operator
δt	Lattice timestep
ε	Porosity
ν	Kinematic viscosity m^2/s
μ	Dynamic viscosity, N m^{-2} s
ρ	Density
ω	Weight function
τ	Dimensionless single relaxation time for the flow computation

Subscripts

f	Fluid flow field
i	Move the direction of single particle
in	Inlet
out	Outlet
p	Pore area
s	Solid area
tot	Total
w	Wall

Superscripts

eq	Equilibrium
neq	Non-equilibrium

References

1. Mahmoudi, Y.; Hooman, K.; Vafai, K. *Convective Heat Transfer in Porous Media*; CRC Press: Boca Raton, FL, USA, 2019.
2. Das, M.K.; Mukherjee, P.P.; Muralidhar, K. *Modeling Transport Phenomena in Porous Media with Applications*; Springer International Publishing: New York, NY, USA, 2018.
3. Mahdi, R.A.; Mohammed, H.; Munisamy, K.; Saeid, N. Review of convection heat transfer and fluid flow in porous media with nanofluid. *Renew. Sustain. Energy Rev.* **2015**, *41*, 715–734. [CrossRef]
4. Amini, S.; Mohaghegh, S.J. Application of machine learning and artificial intelligence in proxy modeling for fluid flow in porous media. *Fluids* **2019**, *4*, 126. [CrossRef]
5. Lasseux, D.; Valdés-Parada, F.; Wood, B.J. Recent developments in upscaling and characterization of flow and transport in porous media. *Adv. Water Resour.* **2021**, *150*, 1–5. [CrossRef]
6. Barrande, M.; Bouchet, R.; Denoyel, R. Tortuosity of porous particles. *Anal. Chem.* **2007**, *79*, 9115–9121. [CrossRef] [PubMed]
7. Gasow, S.; Lin, Z.; Zhang, H.C.; Kuznetsov, A.V.; Avila, M.; Jin, Y.J. Effects of pore scale on the macroscopic properties of natural convection in porous media. *J. Fluid Mech.* **2020**, *891*, A25. [CrossRef]
8. Lautenschlaeger, M.P.; Weinmiller, J.; Kellers, B.; Danner, T.; Latz, A. Homogenized lattice Boltzmann model for simulating multi-phase flows in heterogeneous porous media. *Adv. Water Resour.* **2022**, *170*, 104320. [CrossRef]
9. Guo, Z.; Shu, C. *Lattice Boltzmann Method and Its Application in Engineering*; World Scientific: Singapore, 2013.
10. Guo, Z.; Zhao, T.J. A lattice Boltzmann model for convection heat transfer in porous media. *Numer. Heat Transf. Part B* **2005**, *47*, 157–177. [CrossRef]
11. Krüger, T.; Kusumaatmaja, H.; Kuzmin, A.; Shardt, O.; Silva, G.; Viggen, E.M. *The Lattice Boltzmann Method*; Springer: Berlin/Heidelberg, Germany, 2017; Volume 10, pp. 4–15.
12. D'Orazio, A.; Succi, S. Boundary conditions for thermal lattice Boltzmann simulations. In Proceedings of the Computational Science—ICCS 2003: International Conference, Melbourne, Australia and St. Petersburg, Russia, 2–4 June 2003; Proceedings, Part I 3. Springer: Berlin/Heidelberg, Germany, 2003; pp. 977–986.
13. Guo, Z.; Zheng, C.; Shi, B. Non-equilibrium extrapolation method for velocity and pressure boundary conditions in the lattice Boltzmann method. *Chin. Phys.* **2002**, *11*, 366.
14. Norouzi, S.; Soleimani, R.; Vasheghani Farahani, M.; Rasaei, M.R. Pore-scale simulation of capillary force effect in water-oil immiscible displacement process in porous media. In Proceedings of the 81st EAGE Conference and Exhibition 2019, London, UK, 3–6 June 2019; EAGE Publications BV: Bunnik, The Netherlands, 2019; Volume 2019, pp. 1–5.

15. Dorschner, B.; Bösch, F.; Chikatamarla, S.S.; Boulouchos, K.; Karlin, I.V.J. Entropic multi-relaxation time lattice Boltzmann model for complex flows. *J. Fluid Mech.* **2016**, *801*, 623–651. [CrossRef]

16. Succi, S.; Foti, E.; Higuera, F. Three-Dimensional Flows in Complex Geometries with the Lattice Boltzmann Method. *Europhys. Lett. (EPL)* **1989**, *10*, 433–438. [CrossRef]

17. Soleimani, R.; Zargartalebi, M.; Azaiez, J.; Gates, I.D. Hydrodynamic analysis of nanofluid's convective heat transfer in channels with extended surfaces. *Phys. Fluids* **2021**, *33*, 012011. [CrossRef]

18. Vasheghani Farahani, M.; Mousavi Nezhad, M. On the effect of flow regime and pore structure on the flow signatures in porous media. *Phys. Fluids* **2022**, *34*, 115139. [CrossRef]

19. Mahmoudi, S.; Ayatollahi, S.; Jamshidi, S.; Raoof, A. Investigation on reactive flow through porous media by quadtree Lattice Boltzmann. *J. Nat. Gas Sci. Eng.* **2022**, *104*, 104674. [CrossRef]

20. Psihogios, J.; Kainourgiakis, M.; Yiotis, A.; Papaioannou, A.T.; Stubos, A. A lattice Boltzmann study of non-Newtonian flow in digitally reconstructed porous domains. *Transp. Porous Media* **2007**, *70*, 279–292. [CrossRef]

21. Parvan, A.; Jafari, S.; Rahnama, M.; Raoof, A. Insight into particle retention and clogging in porous media; a pore scale study using lattice Boltzmann method. *Adv. Water Resour.* **2020**, *138*, 103530. [CrossRef]

22. Han, Y.; Cundall, P.A.J. Lattice Boltzmann modeling of pore-scale fluid flow through idealized porous media. *Int. J. Numer. Methods Fluids* **2011**, *67*, 1720–1734. [CrossRef]

23. Ramstad, T.; Berg, C.F.; Thompson, K.J. Pore-scale simulations of single-and two-phase flow in porous media: Approaches and applications. *Transp. Porous Media* **2019**, *130*, 77–104. [CrossRef]

24. Feng, X.-B.; Liu, Q.; He, Y.-L. Numerical simulations of convection heat transfer in porous media using a cascaded lattice Boltzmann method. *Int. J. Heat Mass Transf.* **2020**, *151*, 119410. [CrossRef]

25. Fuchsberger, J.; Aigner, P.; Niederer, S.; Plank, G.; Schima, H.; Haase, G.; Karabelas, E. On the incorporation of obstacles in a fluid flow problem using a Navier–Stokes–Brinkman penalization approach. *J. Comput. Sci.* **2022**, *57*, 101506. [CrossRef]

26. Mößner, M.; Radespiel, R. Flow simulations over porous media—Comparisons with experiments. *Comput. Fluids* **2017**, *154*, 358–370. [CrossRef]

27. Graczyk, K.M.; Matyka, M. Predicting porosity, permeability, and tortuosity of porous media from images by deep learning. *Sci. Rep.* **2020**, *10*, 21488. [CrossRef] [PubMed]

28. Wagner, A.; Eggenweiler, E.; Weinhardt, F.; Trivedi, Z.; Krach, D.; Lohrmann, C.; Jain, K.; Karadimitriou, N.; Bringedal, C.; Voland, P.; et al. Permeability estimation of regular porous structures: A benchmark for comparison of methods. *Transp. Porous Media* **2021**, *138*, 1–23. [CrossRef]

29. Marafini, E.; La Rocca, M.; Fiori, A.; Battiato, I.; Prestininzi, P. Suitability of 2D modelling to evaluate flow properties in 3D porous media. *Transp. Porous Media* **2020**, *134*, 315–329. [CrossRef]

30. Espinoza-Andaluz, M.; Moyón, A.; Andersson, M. A comparative study between D2Q9 and D2Q5 lattice Boltzmann scheme for mass transport phenomena in porous media. *Comput. Math. Appl.* **2019**, *78*, 2886–2896. [CrossRef]

31. Bear, J. *Dynamics of Fluids in Porous Media*; Courier Corporation: Chelmsford, MA, USA, 2013.

32. Zhang, M.; Ye, G.; van Breugel, K. Microstructure-based modeling of permeability of cementitious materials using multiple-relaxation-time lattice Boltzmann method. *Comput. Mater. Sci.* **2013**, *68*, 142–151. [CrossRef]

33. Guo, Z.; Zhao, T. Lattice Boltzmann model for incompressible flows through porous media. *Phys. Rev. E* **2002**, *66*, 036304. [CrossRef]

34. Chen, S.; Doolen, G.D. Lattice Boltzmann method for fluid flows. *Annu. Rev. Fluid Mech.* **1998**, *30*, 329–364. [CrossRef]

35. Liu, W.; Wu, C.-Y. Modelling Complex Particle–Fluid Flow with a Discrete Element Method Coupled with Lattice Boltzmann Methods (DEM-LBM). *Chem. Eng.* **2020**, *4*, 55. [CrossRef]

36. Peng, Y.; Shu, C.; Chew, Y. Simplified thermal lattice Boltzmann model for incompressible thermal flows. *Phys. Rev. E* **2003**, *68*, 026701. [CrossRef]

37. Zhao, T.; Zhao, H.; Ning, Z.; Li, X.; Wang, Q. Permeability prediction of numerical reconstructed multiscale tight porous media using the representative elementary volume scale lattice Boltzmann method. *Int. J. Heat Mass Transf.* **2018**, *118*, 368–377. [CrossRef]

38. Zou, Q.; He, X. On pressure and velocity boundary conditions for the lattice Boltzmann BGK model. *Phys. Fluids* **1997**, *9*, 1591–1598. [CrossRef]

39. Maier, R.S.; Bernard, R.S.; Grunau, D.W.J. Boundary conditions for the lattice Boltzmann method. *Phys. Fluids* **1996**, *8*, 1788–1801. [CrossRef]

40. Mora, C.A.; Wattenbarger, R.A. Analysis and verification of dual porosity and CBM shape factors. *J. Can. Pet. Technol.* **2009**, *48*, 17–21. [CrossRef]

41. Shuja, S.Z.; Yilbas, B.S.; Khan, S.M. Flow subjected to porous blocks in the cavity: Consideration of block aspect ratio and porosity. *Chem. Eng. J.* **2008**, *139*, 84–92. [CrossRef]

42. Wu, C.; Zhang, T.; Fu, J.; Liu, X.; Shen, B. Random pore structure and REV scale flow analysis of engine particulate filter based on LBM. *Open Phys.* **2020**, *18*, 881–896. [CrossRef]